atoms

MDPI

Article

Integral Cross Sections and Transport Properties for Positron–Radon Scattering over a Wide Energy Range (0–1000 eV) and Reduced Electric Field Range (0.01–1000 Td)

Gregory J. Boyle [1,*], Dale L. Muccignat [1], Joshua R. Machacek [2] and Robert P. McEachran [2]

[1] College of Science and Engineering, James Cook University, Townsville, QLD 4810, Australia; dale.muccignat@my.jcu.edu.au
[2] Research School of Physics, Australian National University, Canberra, ACT 0200, Australia; joshua.machacek@anu.edu.au (J.R.M.); robert.mceachran@anu.edu.au (R.P.M.)
* Correspondence: gregory.boyle@my.jcu.edu.au

Abstract

We present fully relativistic calculations of integral cross sections and swarm transport properties for positron–radon scattering over a wide energy range (0–1000 eV) and reduced electric field range (0.01–1000 Td). Elastic (total, momentum-transfer and viscosity-transfer), discrete excitation, direct annihilation, positronium formation and positron-impact ionization cross sections are obtained using a complex relativistic optical potential method. Owing to the large atomic number of radon and the absence of experimental scattering data, a consistent relativistic treatment is essential. The present work provides the first fully relativistic, internally consistent cross-section dataset for positron swarms in radon gas. Using a multi-term solution of Boltzmann's equation, steady-state transport coefficients are calculated and found to be strongly influenced by energy-dependent reactive loss, particularly positronium formation. Significant divergence between bulk and flux transport coefficients is observed, including non-monotonic bulk drift velocities and pronounced suppression of longitudinal bulk diffusion at intermediate fields (0.3–1000 Td). Time-dependent field-free calculations further quantify thermalization and annihilation dynamics through the evolution of the mean energy and $\langle Z_{\mathrm{eff}} \rangle (t)$. These results provide a robust theoretical foundation for modelling positron transport and annihilation in radon and other heavy noble gases where relativistic and reactive effects are crucial.

Keywords: radon; positron scattering; positron transport

Check for updates

Academic Editor: Sabyasachi Kar

Received: 6 March 2026
Revised: 16 April 2026
Accepted: 20 April 2026
Published: 23 April 2026

Copyright: © 2026 by the authors. Licensee MDPI, Basel, Switzerland. This article is an open access article distributed under the terms and conditions of the Creative Commons Attribution (CC BY) license.

1. Introduction

Noble gases, with their closed-shell electronic structure, provide ideal benchmark systems for testing theoretical methods describing low-energy lepton–atom interactions. Over the past several decades, extensive experimental and theoretical studies [1–4] have established a detailed understanding of positron and electron scattering from the lighter noble gases, particularly helium, neon, argon, krypton and xenon. In these systems, comparisons between high-precision measurements and sophisticated theoretical approaches have enabled stringent tests of polarization, exchange and correlation effects.

Radon is the heaviest naturally occurring noble gas and represents an extreme member of this isoelectronic sequence. Owing to its large atomic number, relativistic effects play a dominant role in determining its electronic structure and scattering dynamics [5,6]. For example, strong spin–orbit splitting leads to substantial fine-structure separations in

the low-lying excited states. Despite its fundamental interest, radon remains experimentally inaccessible for scattering studies due to its radioactivity and short half-life, as well as the toxicity of its decay products. Consequently, there are currently no experimental data for either electron or positron scattering from radon, and reliable theoretical predictions are essential.

Radon is produced naturally through the radioactive decay chain of uranium, and its spatial distribution is therefore strongly governed by local geology. Although radon is unlikely to find application in conventional gaseous electronic devices due to its radioactivity, knowledge of its transport properties provides a stringent test of theoretical predictive capability for heavy atomic systems. Furthermore, such data may be relevant in geophysical and environmental contexts, including subsurface gas transport, resource exploration, and seismic monitoring, where radon is commonly used as a tracer species [7,8].

Positron scattering differs qualitatively from electron scattering through the presence of annihilation and positronium (Ps) formation channels, and the absence of the exchange process [9,10]. The reactive processes introduce strong energy-dependent loss mechanisms that can significantly alter both the scattering cross sections and the resulting transport behavior. In particular, Ps formation provides an additional inelastic pathway that can dominate the collision dynamics once energetically accessible. For heavy targets such as radon, where polarization and relativistic effects are pronounced, a consistent and fully relativistic treatment of these processes is especially important.

While previous theoretical work has investigated positron–radon scattering using semi-relativistic optical potential methods [11], a fully relativistic and internally consistent treatment of elastic, excitation, ionization, annihilation and positronium-formation processes has not been reported. Very recently, electron scattering from radon has been reported by the authors [12], demonstrating the importance of a fully relativistic treatment for this heavy target. The present study naturally extends this approach to positron scattering, where the consequences of such cross sections for positron swarm transport in radon gas remain previously unexplored. Swarm transport calculations provide a powerful framework for linking microscopic cross sections to macroscopic observables such as drift velocity, diffusion coefficients and annihilation rates, and are essential for modelling positron behavior in gaseous environments [13–15].

In this work, we present comprehensive calculations of integral cross sections for positron–radon scattering over the energy range 0–1000 eV using a complex relativistic optical potential (ROP) method [6]. The calculated cross sections are then employed in a multi-term solution of Boltzmann's equation [13,16,17] to determine steady-state transport coefficients over reduced electric fields from 0.01 to 1000 Td. We also investigate field-free thermalization and annihilation dynamics through time-dependent calculations of the mean energy and effective annihilation parameter $\langle Z_{\mathrm{eff}} \rangle (t)$. The results provide the first fully relativistic cross section and transport dataset for positron swarms in radon and demonstrate the pronounced influence of energy-dependent reactive loss processes on positron transport in heavy noble gases.

2. Theoretical Scattering and Transport Simulation Details

2.1. Cross Sections

Elastic and inelastic positron–radon scattering cross sections were calculated using the fully relativistic optical potential (ROP) method of Chen et al. [6]. This approach is based on an approximate solution of the relativistic close-coupling equations formulated within the Dirac–Fock framework. The method has recently been applied successfully to electron scattering from radon, and we refer the reader to Refs. [6,18] for comprehensive details. Only a concise summary is provided here.

The scattering of a positron with wave number k from a radon atom is described by the integral-equation form of the partial-wave Dirac–Fock scattering equations. In the ROP formulation, these may be written in matrix form as

$$\begin{pmatrix} F_\kappa(r) \\ G_\kappa(r) \end{pmatrix} = \begin{pmatrix} v_1(kr) \\ v_2(kr) \end{pmatrix} + \frac{1}{k}\int_0^r G(r,x)\left[U(x) - iU_{\mathrm{opt}}(x)\right]\begin{pmatrix} F_\kappa(x) \\ G_\kappa(x) \end{pmatrix} dx, \tag{1}$$

where F_κ and G_κ are the large and small components of the relativistic scattering wavefunction, v_1 and v_2 are free-particle solutions expressed in terms of Riccati–Bessel functions, and $G(r,x)$ is the free-particle Green function. All the wavefunctions were obtained numerically from the relativistic wavefunction program of Grant et al. [5].

For positron scattering, the real local potential is given by

$$U(r) = U_{\mathrm{st}}(r) + U_{\mathrm{pol}}(r), \tag{2}$$

where $U_{\mathrm{st}}(r)$ is the static Dirac–Fock potential obtained from the ground-state atomic wavefunctions of radon, and $U_{\mathrm{pol}}(r)$ is a local polarization potential. The polarization potential includes the first eight multipole contributions (excluding monopole), determined using the polarized-orbital method of McEachran et al. [3]. This construction ensures a consistent relativistic description of polarization effects, which are particularly important for heavy atoms such as radon. These polarization potentials are all zero at the origin and behave asymptotically as $\frac{\alpha_\nu}{2r^{2\nu+2}}$. Here α_ν is the multipole polarization potential and ν is the order of the multipole (i.e., $\nu = 1$ corresponds to the dipole potential).

The imaginary component of the optical potential, $U_{\mathrm{opt}}(r)$, accounts for inelastic processes via absorption of incident flux into excitation, ionization and positronium-formation channels. It is constructed from sums and integrations over discrete and continuum Dirac–Fock states of the atom (see Equation (21b) of Ref. [6] for details). In the present implementation, the real part of the original optical potential is replaced by the explicit polarization potential described above, so that U_{opt} represents purely the absorptive contribution [4].

The elastic and inelastic cross sections are obtained from the complex phase shifts

$$\eta_l^{\pm}(k) = \delta_l^{\pm}(k) + i\gamma_l^{\pm}(k), \tag{3}$$

where the superscripts $\pm$ denote the relativistic spin–orbit components. The integrated elastic cross section is given by

$$\sigma_{\mathrm{el}}(k^2) = \frac{2\pi}{k^2}\sum_{l=0}^{\infty}\Big[(l+1)e^{-2\gamma_l^+}\left(\cosh 2\gamma_l^+ - \cos 2\delta_l^+\right) + le^{-2\gamma_l^-}\left(\cosh 2\gamma_l^- - \cos 2\delta_l^-\right)\Big], \tag{4}$$

while the total inelastic (absorption) cross section is

$$\sigma_{\mathrm{inel}}(k^2) = \frac{\pi}{k^2}\sum_{l=0}^{\infty}\left[(l+1)(1-e^{-4\gamma_l^+}) + l(1-e^{-4\gamma_l^-})\right]. \tag{5}$$

For positron scattering, exchange effects are absent, and all phase shifts vanish as $k \to 0$. Nevertheless, the scattering length remains finite, leading to a non-zero elastic cross

section in the zero-energy limit. The purely elastic regime extends from threshold up to the positronium-formation energy at 3.95 eV.

2.2. Direct Annihilation

Direct annihilation arises from the overlap of the incident positron wavefunction with the target electron density, leading predominantly to 2γ decay. The annihilation rate is expressed in terms of the effective electron number Z_{eff}, which quantifies the electron density sampled by the positron. In the polarized-orbital framework [3], Z_{eff} is obtained from the positron–atom wavefunction via a contact-density integral over all electrons. The corresponding cross section is

$$\sigma_{\text{ann}} = \pi r_0^2 \frac{c}{v} Z_{\text{eff}}, \tag{6}$$

where r_0 is the classical electron radius and v is the positron velocity. In the present work, σ_{ann} is calculated using the relativistic ROP scattering wavefunctions, which account for the distortion of the positron wavefunction and the resulting low-energy enhancement of the annihilation probability.

2.3. Excitation and Ionization

Inelastic excitation and direct ionization processes are incorporated through the absorptive component of the optical potential, constructed from discrete and continuum Dirac–Fock states of radon.

Eight low-lying bound excited states were included explicitly in the absorption potential, namely $7s[3/2]_1$, $7s[1/2]_1$, $7p[1/2]_0$, $7p[5/2]_2$, $7p[3/2]_2$, $6d[1/2]_1$, $6d[3/2]_1$ and $6d[7/2]_3$. These states correspond to dipole-allowed and dominant quadrupole transitions from the ground configuration and therefore provide the leading contributions to discrete excitation. Here the excitation and ionization threshold energies were taken from the NIST database [19].

Continuum states with orbital angular momenta $l_c = 0$–4 were included to simulate direct ionization of the outer-shell 6p, $6\bar{p}$ and 7s electrons. The integration over the continuum spectrum in the absorption potential was performed using a 16-point Gauss–Legendre quadrature.

Within the relativistic close-coupling framework, the total angular momentum J of the positron–atom system is conserved. Consequently, the total angular momentum of the excited (bound or continuum) electron must be coupled to that of the incident positron. This procedure leads to a maximum of 30 discrete excitation channels and 198 ionization channels contributing to the absorption potential.

The excitation cross section reported in this work corresponds to the sum of the individual cross sections from the ground state to each of the eight discrete excited states listed above. Physically, this represents transitions in which a 6p or $6\bar{p}$ electron is promoted to one of the specified excited configurations. The direct ionization cross section corresponds to processes in which both the incident positron and the ejected target electron emerge in the continuum.

2.4. Positronium Formation

Positronium (Ps) formation was incorporated following the approach of McEachran and Stauffer [20], which is a modification of the method originally proposed by Reid and Wadehra [21]. In this framework, the Ps formation cross section is obtained by comparing direct ionization cross sections calculated with two different effective threshold energies.

Specifically, the direct ionization cross section is first calculated using the physical ionization thresholds of radon. A second calculation is then performed in which the

ionization thresholds are reduced by 6.77 eV, corresponding to the binding energy of ground-state positronium. The Ps formation cross section is taken as the difference between these two ionization cross sections. This procedure effectively accounts for the capture of a target electron into a bound positronium state while conserving energy.

As with any simulation-based treatment of Ps formation, the method contains an adjustable high-energy parameter that governs the asymptotic behavior of the cross section. For the noble gases, this parameter is conventionally chosen to be 120 eV + E_{ion}. Importantly, this parameter primarily affects the high-energy tail of the Ps formation cross section and has negligible influence on its threshold behavior or peak magnitude. Since the transport properties of interest are dominated by low- (<3 eV) and intermediate-energy (3–100 eV) collisions, the calculated swarm coefficients are largely insensitive to this choice.

The threshold for ground-state Ps formation in radon occurs at 3.95 eV, corresponding to the difference between the first ionization energy and the positronium binding energy. In the energy interval 3.95–6.77 eV (the Ore gap, i.e., the energy range between Ps formation at 3.95 eV and the first excitation threshold at 6.77 eV), Ps formation is the only energetically accessible inelastic channel. At higher energies, discrete excitation and eventually direct ionization processes also become allowed, leading to competition between inelastic channels.

2.5. Comparison of the ROP and OPM Methods

Both the relativistic optical potential (ROP) method employed in the present work and the optical model potential (OPM) approach used by Khandker et al. [11] are formulated within a Dirac-based scattering framework. However, the physical construction of the interaction potentials and the treatment of inelastic processes differ significantly between the two approaches.

In the ROP method, the real interaction potential comprises a static Dirac–Fock potential supplemented by a polarization potential constructed from the first eight multipole contributions (excluding monopole), determined using atomic wavefunctions and their first-order polarized corrections. This yields a fully relativistic and internally consistent description of polarization effects. In contrast, the OPM approach employs just a dipole polarization potential based on the Buckingham form, which contains an adjustable parameter.

The treatment of inelastic processes also differs fundamentally. In the ROP framework, the absorptive (imaginary) potential is derived explicitly from discrete and continuum Dirac–Fock states of the atom, providing a microscopic representation of excitation, ionization and Ps-formation channels. The OPM method instead incorporates inelastic effects through a semi-relativistic optical potential of Salvat [22], which does not resolve individual inelastic channels explicitly.

The importance of a fully relativistic treatment is particularly pronounced for radon. As a heavy atom, radon exhibits strong spin–orbit splitting and substantial relativistic contraction and expansion of its orbitals. For example, the fine-structure separation of the low-lying 7s and 7p states is several electron volts [23]. Since the ROP method consistently employs relativistic atomic wavefunctions in constructing both polarization and absorption potentials, it is expected to provide a more reliable representation of positron–radon scattering than semi-relativistic approaches.

2.6. Transport Simulations

The positron transport coefficients presented in this work were obtained from a multi-term solution of Boltzmann's equation, following the methodology described in Refs. [13,16,17]. Only a brief outline is provided here.

In the presence of a spatially uniform electric field $\mathbf{E}$, the phase-space distribution function $f(\mathbf{r}, \mathbf{v}, t)$ satisfies

$$\frac{\partial f}{\partial t} + \mathbf{v} \cdot \nabla f + \frac{e\mathbf{E}}{m_p} \cdot \frac{\partial f}{\partial \mathbf{v}} = -J(f), \tag{7}$$

where e and m_p denote the positron charge and mass, respectively, and $J(f)$ is the collision operator incorporating elastic scattering, discrete excitation, ionization, direct annihilation and Ps formation.

Assuming weak spatial gradients, the distribution function may be expanded in terms of the positron number density $n(\mathbf{r}, t)$ via the density-gradient expansion [24],

$$f(\mathbf{r}, \mathbf{v}, t) = nF(\mathbf{v}) - \mathbf{F}^{(1)}(\mathbf{v}) \cdot \nabla n + \mathbf{F}^{(2)}(\mathbf{v}) : \nabla\nabla n + \cdots . \tag{8}$$

This expansion separates the velocity dependence from the spatial evolution of the swarm.

The velocity dependence of each coefficient is further expanded in spherical harmonics. In practice, we employ a Legendre polynomial expansion,

$$F(\mathbf{v}) = \sum_{l=0}^{\infty} F_l(v) P_l(\cos\theta), \tag{9}$$

with analogous expansions for higher-order terms. Here θ is the angle between the velocity vector and the electric field direction. Substitution into Boltzmann's equation yields a hierarchy of coupled differential equations for the expansion coefficients [25].

A full multi-term solution is obtained by truncating the expansion at $l_{\max}$ and increasing $l_{\max}$ until convergence of the transport coefficients is achieved. In the present work, convergence within 0.5 % over the full reduced electric field range was obtained for $l_{\max} = 9$. The necessity of a multi-term treatment arises from the strong anisotropy induced by inelastic and reactive processes, particularly Ps formation, which renders the conventional two-term approximation insufficient (see Section 2.5).

From the converged solution, the flux transport coefficients are calculated as

$$\varepsilon = 2\pi m_p \int_0^{\infty} v^4 F_0(v)\, dv, \tag{10}$$

$$W = \frac{4\pi}{3} \int_0^{\infty} v^3 F_1(v)\, dv, \tag{11}$$

$$D^{L,T} = \frac{4\pi}{3} \int_0^{\infty} v^3 F_1^{L,T}(v)\, dv, \tag{12}$$

where ε is the mean energy, W is the flux drift velocity, and D^L and D^T are the flux longitudinal and transverse diffusion coefficients, respectively.

In systems with non-conservative processes, it is essential to distinguish between flux and bulk transport coefficients. Flux coefficients describe the average motion of individual positrons, whereas bulk coefficients characterize the evolution of the swarm's center of mass. The two are related by correction terms involving the reactive collision frequency $\nu_R(v)$ (see Refs. [25,26]):

$$W_B = W - 4\pi \int_0^{\infty} v^2 \nu_R(v) F_1(v) dv, \tag{13}$$

$$D_B^L = D^L - \frac{4\pi}{\sqrt{3}} \int_0^{\infty} v^2 \nu_R(v) \left[F_0^{2T}(v) - \sqrt{2} F_0^{2L}(v)\right] dv, \tag{14}$$

$$D_B^T = D^T - \frac{4\pi}{\sqrt{3}} \int_0^{\infty} v^2 \nu_R(v) \left[F_0^{2T}(v) + \frac{\sqrt{2}}{2} F_0^{2L}(v)\right] dv. \tag{15}$$

For radon, the reactive collision frequency is

$$\nu_R(v) = Nv[\sigma_{\text{ann}}(v) + \sigma_{\text{Ps}}(v)], \tag{16}$$

where N is the gas number density, and σ_{ann} and σ_{Ps} are the direct annihilation and Ps-formation cross sections. These reactive channels strongly influence bulk transport properties and may produce qualitative differences between bulk and flux coefficients.

Finally, the average effective electron number $\langle Z_{\text{eff}} \rangle$ is obtained from

$$\langle Z_{\text{eff}} \rangle = 4\pi \int_0^\infty \frac{\nu_{\text{ann}}(v)}{\pi r_0^2 c n_0} F_0(v) v^2 dv, \tag{17}$$

where r_0 is the classical electron radius and ν_{ann} is the energy-dependent annihilation frequency. This quantity is directly proportional to the experimentally measurable 2γ annihilation rate [1,27]. An analogous expression may be written in terms of the Ps-formation collision frequency ν_{Ps}, which is sometimes expressed in the literature as an effective annihilation parameter $\langle {}_1Z_{\text{eff}} \rangle$ [2,27,28]. Although Ps formation and direct annihilation are physically distinct processes, both contribute to the overall disappearance rate of positrons from the swarm and therefore influence bulk transport properties and experimentally inferred annihilation characteristics.

3. Results and Discussion

3.1. Cross Sections

The calculated positron–radon cross sections obtained using the ROP method described in Section II are shown in Figure 1 and tabulated in Table 1. Results are presented for the elastic total cross section, momentum-transfer cross section (MTCS), viscosity-transfer cross section (VTCS), direct annihilation, Ps formation, summed discrete excitation, and positron-impact ionization processes. For comparison, cross sections are digitized from the semi-relativistic OPM calculations of Khandker et al. [11] together with representative empirical models for positronium formation [29] and ionisation [30]. For comparison with the corresponding electron–radon results, the reader is referred to the recent study by the authors in Ref. [12].

The elastic cross sections decrease smoothly with increasing energy and exhibit broadly similar trends in both the ROP and OPM approaches, particularly above approximately 10 eV. The direct annihilation cross section displays the characteristic low-energy enhancement associated with the $1/v$ dependence of the annihilation probability, reflecting the increased interaction time between the positron and the target electrons as the positron velocity decreases.

The direct annihilation cross section for positrons in radon is very similar to that in xenon [18,31]. Across the noble gases from helium to xenon, the cross section increases with atomic number, reflecting the growing electron population. For heavier atoms, however, outer-shell screening limits the contribution of inner electrons, leading to a saturation with increasing atomic size, as observed for xenon and radon.

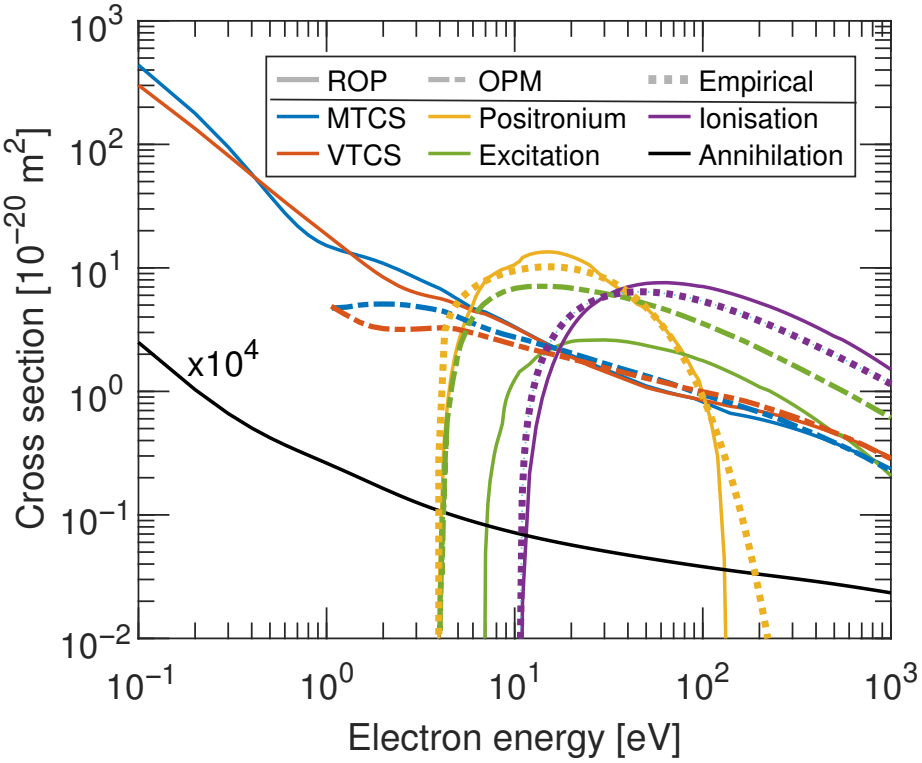


Figure 1. Integral cross sections for positron–radon scattering calculated using the fully relativistic optical potential (ROP) method described in Section 2.1 (solid lines). Displayed are the elastic momentum-transfer (MTCS) and viscosity-transfer (VTCS) cross sections, direct annihilation, positronium formation, summed discrete excitation, and positron-impact ionization over 0–1000 eV. The annihilation cross section is scaled by 10^4 for visibility. Also shown are semi-relativistic optical model potential (OPM) results digitized from Khandker et al. [11] (dash–dot lines), as well as empirical cross sections for positronium formation [29] and ionisation [30] (dotted lines). The OPM VTCS is scaled by 2/3 to account for differing definitions of the viscosity-transfer cross section. The OPM "Excitation" curve represents the total inelastic cross section.

Ps formation becomes energetically accessible at 3.95 eV, corresponding to the difference between the first ionization potential of radon and the 6.77 eV binding energy of ground-state positronium. Above this threshold the Ps formation cross section rises rapidly and dominates the inelastic collision processes within the Ore gap, where no other inelastic channels are energetically available. A noticeable change in slope occurs just below the ionization threshold and corresponds to the onset of excited-state Ps formation, beginning with the $n = 2$ level. Higher excited states ($n = 3$ and $n = 4$) are also accessible below the ionization threshold but contribute only weakly on the scale shown. At higher energies, excitation and subsequently ionization channels open and compete with Ps formation, redistributing the inelastic flux. The empirical models of Machacek et al. [29] and Kim & Rudd [30] produce similar magnitude and energy dependence for Ps formation and ionization respectively, providing additional support for the present ROP results.

Overall, the ROP and OPM elastic cross sections show good qualitative agreement, particularly above approximately 10 eV. However, notable differences arise in the treatment of inelastic processes. The OPM results report only a total inelastic cross section, without resolving excitation, ionization and Ps formation separately. In contrast, the ROP method explicitly distinguishes these channels, allowing a more detailed assessment of their individual contributions. In particular, the ROP positronium-formation cross section is larger than the OPM total inelastic cross section at low and intermediate energies, indicating a significant quantitative difference in the predicted absorption strength.

Table 1. Positron–radon integral cross sections calculated using the fully relativistic ROP method (Section 2.1). Shown are the elastic (Elas.), momentum-transfer (MTCS), viscosity-transfer (VTCS), direct annihilation (Ann.), positronium formation (Ps), excitation (Exc.), and ionization (Ion.) cross sections over 0–1000 eV. All values are given in units of 10^{-20} m^2.

Energy [eV]	Elas.	MTCS	VTCS	Ann.	Ps	Exc.	Ion.
0	2.13×10^{4}	2.13×10^{4}	1.42×10^{4}	∞	0	0	0
1×10^{-3}	1.54×10^{4}	1.54×10^{4}	1.02×10^{4}	6.12×10^{-2}	0	0	0
1×10^{-2}	4.28×10^{3}	4.30×10^{3}	2.86×10^{3}	5.61×10^{-3}	0	0	0
0.1	4.57×10^{2}	4.38×10^{2}	3.02×10^{2}	2.49×10^{-4}	0	0	0
0.2	2.10×10^{2}	1.78×10^{2}	1.34×10^{2}	1.03×10^{-4}	0	0	0
0.3	1.34×10^{2}	9.51×10^{1}	8.12×10^{1}	6.62×10^{-5}	0	0	0
0.4	9.93×10^{1}	5.77×10^{1}	5.66×10^{1}	5.05×10^{-5}	0	0	0
0.5	8.08×10^{1}	3.84×10^{1}	4.28×10^{1}	4.21×10^{-5}	0	0	0
0.6	6.95×10^{1}	2.78×10^{1}	3.42×10^{1}	3.69×10^{-5}	0	0	0
0.7	6.18×10^{1}	2.19×10^{1}	2.84×10^{1}	3.32×10^{-5}	0	0	0
0.8	5.61×10^{1}	1.84×10^{1}	2.42×10^{1}	3.04×10^{-5}	0	0	0
0.9	5.16×10^{1}	1.64×10^{1}	2.11×10^{1}	2.81×10^{-5}	0	0	0
1.0	4.79×10^{1}	1.52×10^{1}	1.86×10^{1}	2.63×10^{-5}	0	0	0
1.2	4.20×10^{1}	1.38×10^{1}	1.50×10^{1}	2.32×10^{-5}	0	0	0
1.4	3.74×10^{1}	1.29×10^{1}	1.25×10^{1}	2.09×10^{-5}	0	0	0
1.6	3.36×10^{1}	1.22×10^{1}	1.07×10^{1}	1.91×10^{-5}	0	0	0
1.8	3.05×10^{1}	1.15×10^{1}	9.35	1.76×10^{-5}	0	0	0
2.0	2.80×10^{1}	1.09×10^{1}	8.40	1.64×10^{-5}	0	0	0
2.2	2.61×10^{1}	1.03×10^{1}	7.79	1.55×10^{-5}	0	0	0
2.4	2.41×10^{1}	9.70	7.18	1.45×10^{-5}	0	0	0
2.6	2.26×10^{1}	9.18	6.79	1.38×10^{-5}	0	0	0
2.8	2.13×10^{1}	8.70	6.50	1.32×10^{-5}	0	0	0
3.0	2.02×10^{1}	8.28	6.27	1.26×10^{-5}	0	0	0
3.2	1.93×10^{1}	7.91	6.10	1.22×10^{-5}	0	0	0
3.4	1.85×10^{1}	7.58	5.96	1.18×10^{-5}	0	0	0
3.6	1.77×10^{1}	7.29	5.85	1.14×10^{-5}	0	0	0
3.8	1.71×10^{1}	7.04	5.75	1.11×10^{-5}	0	0	0
4.0	1.65×10^{1}	6.80	5.65	1.08×10^{-5}	3.75×10^{-2}	0	0
4.2	1.59×10^{1}	6.53	5.54	1.05×10^{-5}	3.60×10^{-1}	0	0
4.4	1.53×10^{1}	6.26	5.42	1.03×10^{-5}	8.13×10^{-1}	0	0
4.6	1.47×10^{1}	6.00	5.30	1.00×10^{-5}	1.34	0	0
4.8	1.42×10^{1}	5.76	5.17	9.82×10^{-6}	1.90	0	0
5.0	1.38×10^{1}	5.56	5.06	9.63×10^{-6}	2.44	0	0
5.2	1.34×10^{1}	5.36	4.94	9.45×10^{-6}	2.99	0	0
5.4	1.30×10^{1}	5.17	4.82	9.29×10^{-6}	3.53	0	0
5.6	1.27×10^{1}	5.00	4.70	9.13×10^{-6}	4.07	0	0
5.8	1.24×10^{1}	4.84	4.59	8.98×10^{-6}	4.58	0	0
6.0	1.22×10^{1}	4.69	4.48	8.85×10^{-6}	5.07	0	0
6.2	1.19×10^{1}	4.35	4.22	8.72×10^{-6}	5.82	0	0
6.4	1.16×10^{1}	4.10	4.01	8.60×10^{-6}	6.37	0	0
6.6	1.14×10^{1}	3.87	3.82	8.48×10^{-6}	6.89	0	0
6.8	1.11×10^{1}	3.66	3.63	8.37×10^{-6}	7.36	0	0
7.0	1.14×10^{1}	4.38	4.22	8.27×10^{-6}	7.97	4.94×10^{-2}	0
7.2	1.13×10^{1}	4.29	4.15	8.17×10^{-6}	8.23	1.22×10^{-1}	0
7.4	1.12×10^{1}	4.20	4.07	8.08×10^{-6}	8.49	1.88×10^{-1}	0
7.6	1.10×10^{1}	4.12	4.00	7.99×10^{-6}	8.73	2.45×10^{-1}	0
7.8	1.09×10^{1}	4.04	3.93	7.90×10^{-6}	8.95	3.11×10^{-1}	0

Table 1. *Cont.*

Energy [eV]	Elas.	MTCS	VTCS	Ann.	Ps	Exc.	Ion.
8.0	1.08×10^{1}	3.97	3.86	7.82×10^{-6}	9.16	3.70×10^{-1}	0
8.2	1.07×10^{1}	3.90	3.80	7.75×10^{-6}	9.36	4.23×10^{-1}	0
8.4	1.06×10^{1}	3.83	3.73	7.67×10^{-6}	9.55	4.78×10^{-1}	0
8.6	1.06×10^{1}	3.76	3.67	7.60×10^{-6}	9.74	5.48×10^{-1}	0
8.8	1.05×10^{1}	3.69	3.61	7.53×10^{-6}	9.83	7.28×10^{-1}	0
9.0	1.04×10^{1}	3.63	3.55	7.47×10^{-6}	9.95	8.55×10^{-1}	0
9.2	1.04×10^{1}	3.56	3.50	7.40×10^{-6}	1.01×10^{1}	9.48×10^{-1}	0
9.4	1.03×10^{1}	3.50	3.44	7.34×10^{-6}	1.02×10^{1}	1.03	0
9.6	1.02×10^{1}	3.44	3.39	7.28×10^{-6}	1.03×10^{1}	1.10	0
9.8	1.02×10^{1}	3.39	3.34	7.23×10^{-6}	1.05×10^{1}	1.17	0
10	1.01×10^{1}	3.33	3.29	7.17×10^{-6}	1.06×10^{1}	1.24	0
11	9.90	3.08	3.05	6.93×10^{-6}	1.21×10^{1}	1.41	1.91×10^{-2}
12	9.70	2.87	2.85	6.72×10^{-6}	1.28×10^{1}	1.66	2.17×10^{-1}
13	9.51	2.69	2.67	6.54×10^{-6}	1.32×10^{1}	1.88	5.20×10^{-1}
14	9.34	2.54	2.52	6.38×10^{-6}	1.34×10^{1}	2.04	8.77×10^{-1}
15	9.16	2.41	2.38	6.23×10^{-6}	1.35×10^{1}	2.16	1.26
16	9.00	2.30	2.26	6.11×10^{-6}	1.34×10^{1}	2.25	1.66
17	8.84	2.20	2.16	5.99×10^{-6}	1.32×10^{1}	2.34	2.08
18	8.68	2.11	2.06	5.89×10^{-6}	1.30×10^{1}	2.42	2.48
19	8.53	2.03	1.98	5.79×10^{-6}	1.27×10^{1}	2.49	2.88
20	8.38	1.96	1.90	5.71×10^{-6}	1.24×10^{1}	2.53	3.25
21	8.23	1.89	1.83	5.63×10^{-6}	1.20×10^{1}	2.57	3.61
22	8.09	1.84	1.77	5.55×10^{-6}	1.16×10^{1}	2.58	3.94
23	7.95	1.76	1.72	5.48×10^{-6}	1.13×10^{1}	2.59	4.25
24	7.81	1.73	1.66	5.42×10^{-6}	1.09×10^{1}	2.59	4.54
25	7.68	1.69	1.62	5.35×10^{-6}	1.06×10^{1}	2.60	4.81
30	8.47	2.36	1.96	5.10×10^{-6}	8.19	2.61	5.87
35	7.93	2.13	1.77	4.89×10^{-6}	6.94	2.58	6.57
40	7.43	1.95	1.62	4.73×10^{-6}	5.93	2.51	7.01
45	6.99	1.81	1.51	4.59×10^{-6}	5.07	2.44	7.30
50	5.47	1.11	1.08	4.48×10^{-6}	4.75	2.35	7.48
55	5.23	1.06	1.04	4.37×10^{-6}	4.11	2.28	7.56
60	5.01	1.02	1.00	4.28×10^{-6}	3.56	2.21	7.59
65	4.83	9.86×10^{-1}	9.75×10^{-1}	4.20×10^{-6}	3.01	2.16	7.59
70	4.68	9.57×10^{-1}	9.51×10^{-1}	4.13×10^{-6}	2.66	2.10	7.53
75	4.54	9.33×10^{-1}	9.30×10^{-1}	4.07×10^{-6}	2.29	2.04	7.47
80	4.42	9.12×10^{-1}	9.12×10^{-1}	4.01×10^{-6}	1.96	1.99	7.39
85	4.32	8.94×10^{-1}	8.95×10^{-1}	3.95×10^{-6}	1.67	1.93	7.30
90	4.23	8.78×10^{-1}	8.78×10^{-1}	3.90×10^{-6}	1.41	1.87	7.21
95	4.19	8.35×10^{-1}	8.86×10^{-1}	3.85×10^{-6}	1.25	1.81	7.11
100	4.12	8.20×10^{-1}	8.75×10^{-1}	3.81×10^{-6}	9.57×10^{-1}	1.77	7.06
110	4.00	7.94×10^{-1}	8.54×10^{-1}	3.73×10^{-6}	5.96×10^{-1}	1.68	6.86
120	3.90	7.70×10^{-1}	8.36×10^{-1}	3.66×10^{-6}	2.96×10^{-1}	1.59	6.64
130	3.81	7.49×10^{-1}	8.19×10^{-1}	3.60×10^{-6}	4.51×10^{-2}	1.50	6.43
140	3.75	6.65×10^{-1}	7.58×10^{-1}	3.55×10^{-6}	0	1.43	6.23
150	3.68	6.53×10^{-1}	7.47×10^{-1}	3.50×10^{-6}	0	1.36	6.04
160	3.63	6.41×10^{-1}	7.36×10^{-1}	3.46×10^{-6}	0	1.30	5.85
170	3.57	6.30×10^{-1}	7.24×10^{-1}	3.41×10^{-6}	0	1.24	5.68
180	3.53	6.18×10^{-1}	7.13×10^{-1}	3.38×10^{-6}	0	1.18	5.51
190	3.48	6.08×10^{-1}	7.03×10^{-1}	3.34×10^{-6}	0	1.13	5.36
200	3.44	5.97×10^{-1}	6.92×10^{-1}	3.31×10^{-6}	0	1.09	5.21

Table 1. *Cont.*

Energy [eV]	Elas.	MTCS	VTCS	Ann.	Ps	Exc.	Ion.
250	3.26	5.48×10^{-1}	6.40×10^{-1}	3.17×10^{-6}	0	9.28×10^{-1}	4.59
300	3.12	5.05×10^{-1}	5.94×10^{-1}	3.06×10^{-6}	0	7.86×10^{-1}	4.09
350	3.00	4.68×10^{-1}	5.53×10^{-1}	2.97×10^{-6}	0	6.76×10^{-1}	3.67
400	2.90	4.35×10^{-1}	5.17×10^{-1}	2.89×10^{-6}	0	5.89×10^{-1}	3.33
450	2.81	4.07×10^{-1}	4.86×10^{-1}	2.82×10^{-6}	0	5.18×10^{-1}	3.04
500	2.73	3.82×10^{-1}	4.58×10^{-1}	2.76×10^{-6}	0	4.60×10^{-1}	2.79
550	2.66	3.60×10^{-1}	4.33×10^{-1}	2.70×10^{-6}	0	4.41×10^{-1}	2.63
600	2.59	3.40×10^{-1}	4.11×10^{-1}	2.65×10^{-6}	0	4.00×10^{-1}	2.44
650	2.53	3.23×10^{-1}	3.91×10^{-1}	2.60×10^{-6}	0	3.64×10^{-1}	2.28
700	2.47	3.07×10^{-1}	3.73×10^{-1}	2.55×10^{-6}	0	3.33×10^{-1}	2.13
750	2.42	2.92×10^{-1}	3.57×10^{-1}	2.51×10^{-6}	0	3.05×10^{-1}	2.00
800	2.37	2.79×10^{-1}	3.42×10^{-1}	2.47×10^{-6}	0	2.82×10^{-1}	1.88
850	2.33	2.67×10^{-1}	3.28×10^{-1}	2.44×10^{-6}	0	2.60×10^{-1}	1.77
900	2.29	2.56×10^{-1}	3.15×10^{-1}	2.40×10^{-6}	0	2.40×10^{-1}	1.67
950	2.25	2.46×10^{-1}	3.04×10^{-1}	2.37×10^{-6}	0	2.24×10^{-1}	1.58
1000	2.21	2.36×10^{-1}	2.93×10^{-1}	2.34×10^{-6}	0	2.08×10^{-1}	1.51

At higher energies (above ∼30 eV), the ROP ionization cross section exceeds the OPM inelastic result, despite the latter nominally including all inelastic channels. This suggests that differences in the construction of the absorption potential lead to appreciable variations in predicted inelastic flux. Given the fully relativistic and state-resolved treatment employed in the ROP framework, these results provide a more physically transparent representation of positron–radon scattering dynamics.

3.2. Transport Properties

3.2.1. Steady-State Calculations

Steady-state transport coefficients for a positron swarm in radon at 293 K were calculated over the reduced electric field range $0.01 \leq E/N \leq 1000$ Td using the ROP cross-section set. Both flux and bulk coefficients are presented in order to quantify the influence of non-conservative processes on swarm dynamics. The results are shown in Figure 2.

The top left panel displays the volumetric reaction rates for direct annihilation, positronium (Ps) formation and positron-impact ionization. At very low reduced electric fields, the annihilation rate is relatively large due to the enhancement of the low-energy annihilation cross section. As E/N increases and the mean positron energy rises, the annihilation rate decreases accordingly. Ps formation becomes energetically accessible once the mean energy exceeds the threshold at 3.95 eV, corresponding to $E/N \approx 0.5$ Td. Above this field strength, Ps formation rapidly dominates the reactive loss processes. Although ionization is energetically allowed at higher fields, it remains a comparatively weak channel over the entire range considered. It should be noted that, for positron swarms, ionization is a particle-conserving process.

The top right panel shows the bulk and flux drift velocities. Even at the lowest field strength considered, the two differ appreciably, reflecting the influence of energy-dependent reactive loss. At very low fields, annihilation preferentially removes slower positrons from the swarm, leading to an increase in the average velocity of the surviving particles (annihilation heating). As E/N increases toward ∼0.1 Td, both drift velocities rise sharply, with the effect being particularly pronounced for the bulk drift velocity. This behavior results from the interplay between field-driven acceleration, elastic momentum transfer and reactive loss, an effect noted by Robson in 1986 [25] for positrons in helium.

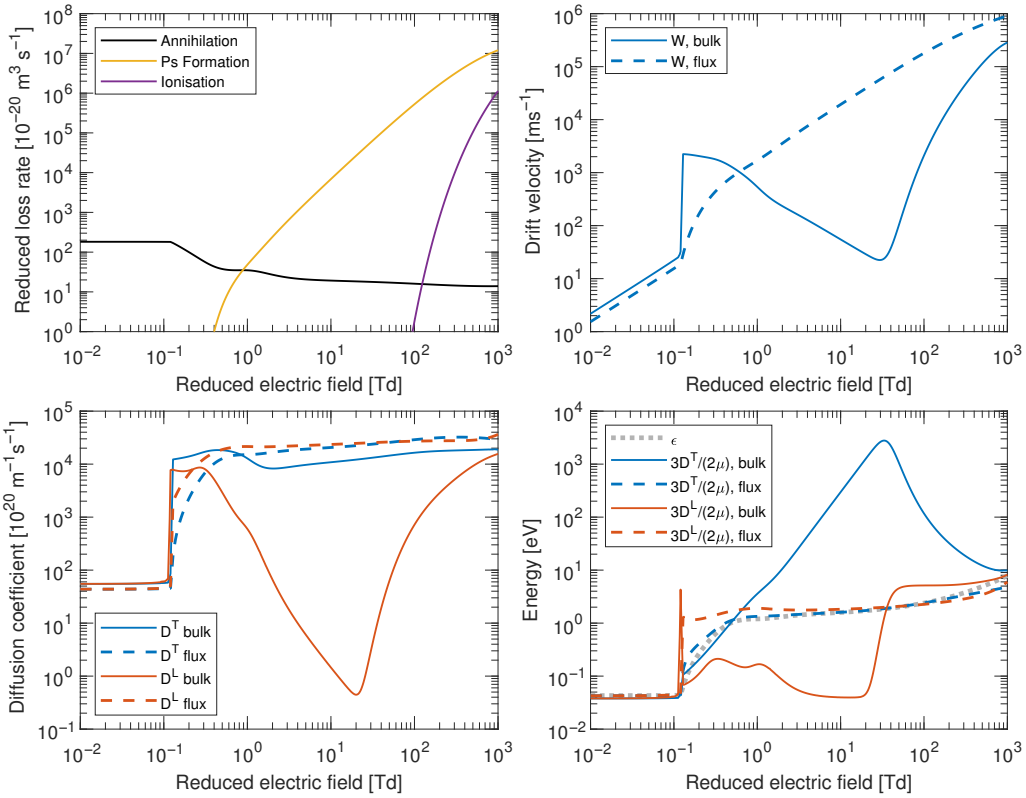


Figure 2. Steady-state positron swarm transport properties in radon at 293 K calculated using the fully relativistic ROP cross section set described in Section 2.1. Results are shown over the reduced electric field range 0.01–1000 Td. (**Top Left**) Volumetric reaction rates for direct annihilation, positronium formation, and positron-impact ionization (the latter being particle-conserving). (**Top Right**) Bulk and flux drift velocities. (**Bottom Left**) Bulk and flux longitudinal and transverse diffusion coefficients. (**Bottom Right**) Mean energy together with longitudinal and transverse characteristic energies.

Beyond this initial rise, the flux drift velocity increases monotonically with E/N, as expected from continued acceleration in the applied field. In contrast, the bulk drift velocity decreases over the range ∼0.1–30 Td before increasing again at higher fields. This non-monotonic behavior is a direct consequence of energy-selective Ps formation, which preferentially removes higher-energy positrons and thereby alters the motion of the swarm centroid. As a result, the bulk drift velocity may exceed or fall below the flux value depending on field strength, demonstrating the qualitative impact of reactive loss on swarm evolution.

The bottom left panel presents the longitudinal and transverse diffusion coefficients in both bulk and flux forms. At very low reduced electric fields ($E/N \lesssim 0.05$ Td), both bulk and flux diffusion coefficients approach approximately constant values. In this regime, the swarm is close to thermal equilibrium with the background gas, and the transport coefficients are governed primarily by elastic momentum-transfer collisions. Reactive losses enhance the bulk components with respect to the flux components.

As E/N increases beyond ∼0.1 Td, both longitudinal and transverse diffusion coefficients exhibit a sharp rise. This increase coincides with the rapid growth in drift velocity and mean energy and observed in the top right and bottom right panels, and reflects the onset of strong field-driven acceleration combined with annihilation heating. As the swarm begins to sample higher energies where the momentum-transfer cross section decreases, the effective collision frequency is reduced, leading to enhanced spatial spreading and hence larger diffusion coefficients.

At higher fields, the flux diffusion coefficients increase smoothly with E/N and eventually converge, consistent with an increasingly anisotropic velocity distribution dominated by elastic scattering. In contrast, the bulk diffusion coefficients exhibit pronounced structure at low and intermediate fields. Most notably, the longitudinal bulk diffusion coefficient decreases by several orders of magnitude between approximately 0.3 and 20 Td. This dramatic suppression reflects strong spatial localization of the swarm caused by energy-dependent positron loss, particularly Ps formation, which preferentially removes higher-energy positrons and reduces the variance of the swarm position along the field direction. The transverse bulk diffusion coefficient displays a similar but less pronounced trend, consistent with the anisotropic influence of the electric field.

The bottom right panel shows the mean energy together with the longitudinal and transverse characteristic energies using both bulk and flux definitions. The mean energy increases quickly near ∼0.1 Td, consistent with the combined effects of annihilation heating and field acceleration. The flux transverse characteristic energy provides a reasonable approximation to the mean energy over much of the field range. The flux longitudinal characteristic energy also provides a reasonable estimate at both very low and high energies, but fails between ∼0.1 and 5 Td. The bulk characteristic energies exhibit extreme variations due to their sensitivity to reactive loss and the non-monotonic bulk drift velocity. These results highlight that bulk characteristic energies do not represent simple thermodynamic measures, but rather reflect the coupled spatial and energetic evolution of a reactive positron swarm.

3.2.2. Multi-Term Convergence

To quantify the influence of velocity–space anisotropy on the calculated transport coefficients, we compared results obtained from the full multi-term solution of Boltzmann's equation using different numbers of Legendre terms.

The two-term approximation is frequently adopted for computational efficiency; however, its limitations in systems exhibiting strong anisotropy or non-conservative processes are well established [32–34]. In the present work, a full multi-term Legendre expansion (Section 2.6) was implemented. The expansion was truncated at progressively higher $l_{\max}$ until all transport coefficients converged to within 0.5 % over the entire reduced electric field range. Global convergence was achieved using $l_{\max} = 9$.

The convergence behaviour at representative reduced electric fields between 0.01 and 1000 Td is summarised in Table 2. At low fields ($E/N = 0.01$ Td to 10 Td), the velocity distribution remains nearly isotropic and the two-term approximation provides an adequate description. As the field increases, generally progressively higher-order angular components become significant. For example, at $E/N = 100$ Td, at least six terms are required to achieve convergence at the 0.5 % level, reflecting increasing anisotropy of the distribution function. At the highest field considered ($E/N = 1000$ Td), convergence requires $l_{\max} = 9$.

The required truncation order is therefore strongly field-dependent. In particular, at $E/N = 1000$ Td the two-term approximation deviates substantially from the converged solution, with discrepancies ranging from approximately 50 % to more than 200 %, depending on the transport quantity considered. Furthermore, the two-term approximation exhibits a nonphysical negative bulk longitudinal diffusion coefficient, which quickly corrects for $l_{\max} \geq 3$. These large deviations arise from the pronounced anisotropy induced by strong field acceleration combined with energy-dependent reactive loss, especially Ps formation.

Table 2. Convergence of select steady-state transport coefficients with increasing spherical harmonic truncation order $l_{\max}$. Values are shown to three significant figures.

E/N [Td]	$l_{\max}$	ϵ [eV]	W_B [m s^{-1}]	D_B^L [10^{20} m^{-1}s^{-1}]	D_B^T [10^{20} m^{-1}s^{-1}]
0.01	1	4.30×10^{-2}	2.18	5.50×10^{1}	5.50×10^{1}
	3	4.30×10^{-2}	2.18	5.50×10^{1}	5.50×10^{1}
0.1	1	4.34×10^{-2}	2.22×10^{1}	6.15×10^{1}	5.73×10^{1}
	3	4.34×10^{-2}	2.22×10^{1}	6.10×10^{1}	5.72×10^{1}
	5	4.34×10^{-2}	2.22×10^{1}	6.10×10^{1}	5.72×10^{1}
1	1	1.20	5.38×10^{2}	5.98×10^{2}	1.28×10^{4}
	3	1.20	5.38×10^{2}	5.98×10^{2}	1.28×10^{4}
10	1	1.59	5.49×10^{1}	1.43	1.09×10^{4}
	3	1.59	5.49×10^{1}	1.44	1.09×10^{4}
100	1	2.42	1.54×10^{3}	5.26×10^{2}	2.19×10^{4}
	3	2.39	2.11×10^{3}	7.22×10^{2}	1.65×10^{4}
	5	2.39	2.10×10^{3}	7.19×10^{2}	1.64×10^{4}
	7	2.39	2.10×10^{3}	7.19×10^{2}	1.64×10^{4}
1000	1	11.8	1.33×10^{6}	-2.60×10^{4}	6.55×10^{4}
	3	8.35	4.98×10^{5}	2.05×10^{4}	1.54×10^{5}
	5	7.91	4.18×10^{5}	2.04×10^{4}	2.86×10^{4}
	7	7.85	4.08×10^{5}	2.04×10^{4}	2.07×10^{4}
	9	7.85	4.07×10^{5}	2.04×10^{4}	1.99×10^{4}
	11	7.85	4.06×10^{5}	2.04×10^{4}	1.99×10^{4}

Such behaviour is consistent with previous investigations of charged-particle swarms in reactive gases [35]. Energy-selective loss mechanisms enhance angular structure in the velocity distribution function, amplifying higher-order Legendre components and often rendering low-order truncations inadequate. Consequently, reliable modelling of positron transport in radon requires a fully converged multi-term framework. This is particularly important for inverse swarm analyses aimed at refining cross sections, where insufficient angular resolution may introduce systematic bias.

3.2.3. Field-Free Thermalization and Annihilation

We now consider field-free positron annihilation and thermalization in radon gas. The experimentally accessible quantity in such studies is the time-dependent effective electron number, $\langle Z_{\text{eff}} \rangle(t)$, which is determined from measurements of the 2γ annihilation intensity as a function of time [1,27].

Thermalization refers to the evolution of the normalized positron energy distribution toward a steady state. This steady state represents a balance between collisional energy exchange with the background gas and energy-selective reactive loss through direct annihilation and positronium (Ps) formation. Because the annihilation and Ps cross sections are strongly energy-dependent, reactive heating and cooling effects may drive the distribution away from a Maxwellian form and produce a steady-state mean energy that differs from the thermal energy of the gas [25,36].

Time-resolved annihilation measurements have previously been performed for positrons in noble gases from helium through xenon; however, no such data are available for radon. Moreover, the initial energy distribution of injected positrons is generally not well characterized. Following Boyle et al. [17], we assume an initial distribution uniform in energy space up to the radon ionization threshold of 10.7 eV, i.e.,

$$\epsilon^{1/2} f_0(\epsilon, 0)\, \Theta(10.7\ \text{eV} - \epsilon) = C, \tag{18}$$

where Θ is the Heaviside function and C is a normalization constant. The sensitivity of the relaxation dynamics to this assumption was examined in Ref. [17].

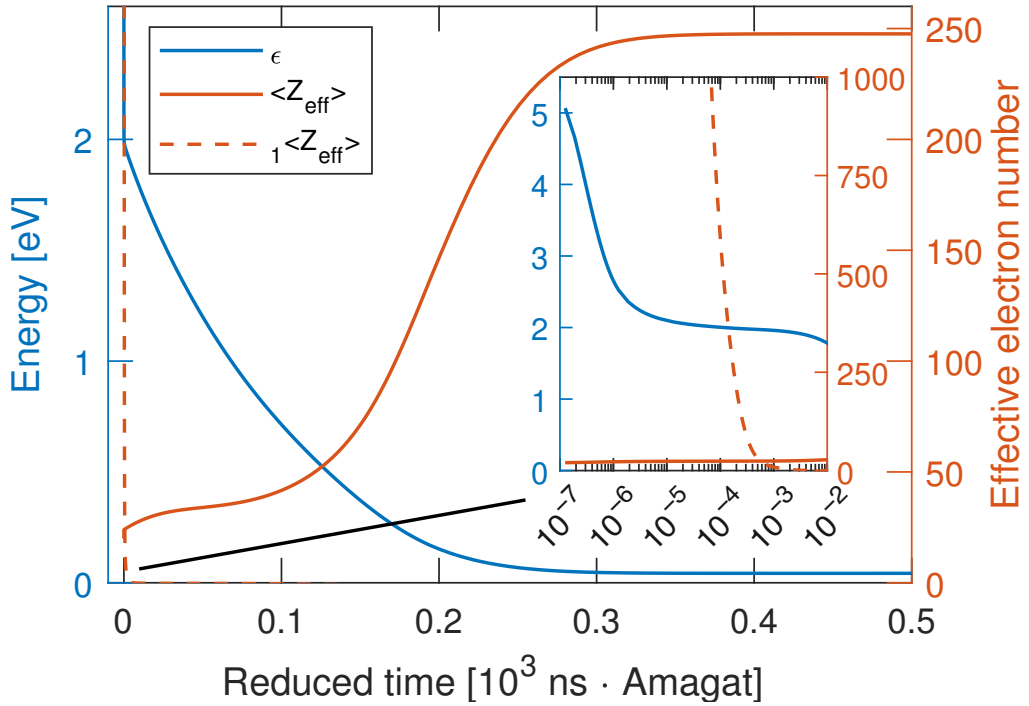


Figure 3. Field-free thermalization of a positron swarm in radon at 293 K. Shown are the temporal evolution of the mean positron energy ϵ and the effective electron numbers $\langle Z_{\text{eff}}\rangle(t)$ (direct annihilation) and ${}_1\langle Z_{\text{eff}}\rangle(t)$ (positronium formation analogue), calculated using the ROP cross-section set. The initial positron energy distribution is uniform in energy space up to the ionization threshold (10.7 eV). The reduced time is expressed in density-scaled units $N \cdot t$ (ns·amagat). The inset highlights the early-time dynamics, where relaxation is dominated by inelastic energy loss through Ps formation.

Figure 3 shows the temporal evolution of the mean positron energy and the corresponding $\langle Z_{\text{eff}}\rangle(t)$ and $\langle Z_{\text{eff}}\rangle_1(t)$ under field-free conditions. The mean energy decreases rapidly from its initial value of 5.35 eV toward the steady-state value of 0.0426 eV, reaching equilibrium on a timescale of approximately 300 ns·amagat. The initial stage of relaxation, highlighted by the figure inset, is dominated by inelastic energy loss, particularly Ps formation, which efficiently removes higher-energy positrons from the swarm. Once the mean energy falls below the Ps formation threshold, inelastic processes are suppressed and subsequent cooling proceeds primarily via elastic momentum-transfer collisions.

The evolution of $\langle Z_{\text{eff}}\rangle(t)$ reflects this changing balance. At early times, the total loss rate is strongly influenced by Ps formation, leading to a rapid decrease in $\langle Z_{\text{eff}}\rangle_1(t)$ as the high-energy portion of the distribution is depleted. As the swarm cools further through elastic collisions and samples progressively lower energies, the direct annihilation cross section increases, and $\langle Z_{\text{eff}}\rangle(t)$ rises gradually toward its steady-state value of 242.

The steady-state $\langle Z_{\text{eff}}\rangle$ in radon is lower than that reported for xenon (approximately 350). As discussed earlier, although the annihilation cross sections for xenon and radon are very similar, reflecting saturation of the annihilation probability with increasing atomic size, differences in the elastic momentum-transfer cross sections modify the steady-state energy distribution. Consequently, the ensemble-averaged sampling of the annihilation cross section differs between the two gases, leading to distinct steady-state $\langle Z_{\text{eff}}\rangle$ values.

The overall relaxation timescale in radon (approximately 300 ns·amagat) is slightly longer than in xenon (approximately 200 ns·amagat). This difference reflects the greater atomic mass of radon and the corresponding reduction in energy transfer per elastic collision, resulting in slower cooling of the positron swarm.

4. Summary

We have presented comprehensive calculations of integral cross sections and swarm transport properties for positron–radon scattering using a fully relativistic optical potential (ROP) framework. Given the large atomic number of radon and the absence of experimental scattering data, a consistent relativistic treatment is essential. The present work provides the first ab initio fully relativistic and internally consistent cross-section and transport dataset for positron swarms in radon gas.

Elastic (total, momentum-transfer and viscosity-transfer), direct annihilation, Ps formation, discrete excitation and positron-impact ionization cross sections were calculated over the energy range 0–1000 eV. Comparison with previous semi-relativistic optical model calculations reveals broadly similar elastic behaviour at intermediate and high energies, but significant quantitative differences in the magnitude and decomposition of inelastic channels, particularly Ps formation.

These cross sections were employed in a multi-term solution of Boltzmann's equation to determine steady-state transport coefficients over reduced electric fields from 0.01 to 1000 Td. The results demonstrate the pronounced influence of energy-dependent reactive loss on positron swarm dynamics. Strong divergence between bulk and flux transport coefficients is observed, including non-monotonic bulk drift velocities and substantial suppression of longitudinal bulk diffusion at intermediate fields (0.3–1000 Td). These features arise from the interplay between field-driven acceleration, elastic momentum transfer and energy-selective positron loss, and highlight the necessity of a fully converged multi-term treatment.

Time-dependent, field-free calculations were also performed to investigate thermalization and annihilation dynamics. The positron mean energy relaxes on a timescale of approximately 300 ns·amagat, with the very early stages dominated by Ps formation. The steady-state effective electron number $\langle Z_{\mathrm{eff}} \rangle$ is found to be lower than in xenon despite similar annihilation cross sections, reflecting differences in the steady-state energy distributions induced by elastic scattering.

Overall, the cross-section set and transport coefficients presented here establish a robust theoretical foundation for modelling positron transport and annihilation in radon and other heavy noble gases, where relativistic structure and reactive processes play a dominant role.

Author Contributions: Conceptualization, J.R.M. and R.P.M.; Data curation, G.J.B., D.L.M., J.R.M. and R.P.M.; Formal analysis, G.J.B. and D.L.M.; Investigation, J.R.M. and R.P.M.; Methodology, G.J.B., J.R.M. and R.P.M.; Project administration, G.J.B., J.R.M. and R.P.M.; Resources, J.R.M. and R.P.M.; Software, G.J.B., D.L.M. and R.P.M.; Validation, G.J.B., D.L.M., J.R.M. and R.P.M.; Visualization, G.J.B., D.L.M., J.R.M. and R.P.M.; Writing—original draft, G.J.B., D.L.M., J.R.M. and R.P.M.; Writing—review & editing, G.J.B., D.L.M., J.R.M. and R.P.M. All authors have read and agreed to the published version of the manuscript.

Funding: This research received no external funding.

Data Availability Statement: A representative selection of data is presented in Table 1. Data will be made available upon reasonable request.

Acknowledgments: The authors also wish to acknowledge the support of the Australian Research Council.

Conflicts of Interest: The authors declare no conflicts of interest.

References

1. Charlton, M. Experimental studies of positrons scattering in gases. *Rep. Prog. Phys.* **1985**, *48*, 737. [CrossRef]
2. Griffith, T.C.; Heyland, G. Experimental aspects of the study of the interaction of low-energy positrons with gases. *Phys. Rep.* **1978**, *39*, 169–277. [CrossRef]
3. McEachran, R.P.; Ryman, A.G.; Stauffer, A.D.; Morgan, D.L. Positron scattering from noble gases. *J. Phys. B At. Mol. Phys.* **1977**, *10*, 663. Correction in *J. Phys. B At. Mol. Phys.* **1978**, *11*, 951. [CrossRef]
4. Bartschat, K.; McEachran, R.P.; Stauffer, A.D. Optical potential approach to electron and positron scattering from noble gases. *J. Phys. B At. Mol. Opt. Phys.* **1988**, *21*, 2789. [CrossRef]
5. Grant, I.; McKenzie, B.; Norrington, P.; Mayers, D.; Pyper, N. An atomic multiconfigurational Dirac-Fock package. *Comput. Phys. Commun.* **1980**, *21*, 207–231. [CrossRef]
6. Chen, S.; McEachran, R.P.; Stauffer, A.D. Ab initio optical potentials for elastic electron and positron scattering from the heavy noble gases. *J. Phys. B At. Mol. Opt. Phys.* **2008**, *41*, 025201. [CrossRef]
7. United Nations Scientific Committee on the Effects of Atomic Radiation. Sources and Effects of Ionizing Radiation. UNSCEAR 2000 Report to the General Assembly, with Scientific Annexes. 2000. Available online: https://www.unscear.org (accessed on 13 April 2026).
8. Nazaroff, W.W.; Nero, A.V. *Radon and Its Decay Products in Indoor Air*; Wiley: New York, NY, USA, 1988.
9. Gribakin, G.F.; Young, J.A.; Surko, C.M. Positron-molecule interactions: Resonant attachment, annihilation, and bound states. *Rev. Mod. Phys.* **2010**, *82*, 2557–2607. [CrossRef]
10. Charlton, M.; Humberston, J.W. *Positron Physics*; Cambridge University Press: Cambridge, UK, 2001.
11. Khandker, M.H.; Haque, A.K.F.; Haque, M.M.; Billah, M.M.; Watabe, H.; Uddin, M.A. Relativistic Study on the Scattering of $e^{\pm}$ from Atoms and Ions of the Rn Isonuclear Series. *Atoms* **2021**, *9*, 59. [CrossRef]
12. Boyle, G.J.; Muccignat, D.L.; Machacek, J.R.; McEachran, R.P. Integral Cross Sections and Transport Properties for Electron–Radon Scattering over a Wide Energy Range (0–1000 eV) and a Reduced Electric Field Range (0.01–1000 Td). *Atoms* **2025**, *13*, 82. [CrossRef]
13. Robson, R.E.; White, R.D.; Hildebrandt, M. *Fundamentals of Charged Particle Transport in Gases and Condensed Matter*; CRC Press: Boca Raton, FL, USA, 2017.
14. Petrović, Z.L.; Suvakov, M.; Nikitović, Z.; Dujko, S.; Sasić, O.; Jovanović, J.; Malović, G.; Stojanović, V. Kinetic phenomena in charged particle transport in gases, swarm parameters and cross section data. *Plasma Sources Sci. Technol.* **2007**, *16*, S1. [CrossRef]
15. White, R.D.; Robson, R.; Dujko, S.; Nicoletopoulos, P.; Li, B. Recent advances in the application of Boltzmann equation and fluid equation methods to charged particle transport in non-equilibrium plasmas. *J. Phys. D Appl. Phys.* **2009**, *42*, 194001. [CrossRef]
16. Boyle, G.J.; Stokes, P.W.; Robson, R.E.; White, R.D. Boltzmann's equation at 150: Traditional and modern solution techniques for charged particles in neutral gases. *J. Chem. Phys.* **2023**, *159*, 024306. [CrossRef]
17. Boyle, G.J.; Casey, M.J.E.; White, R.D.; Mitroy, J. Transport theory for low-energy positron thermalization and annihilation in helium. *Phys. Rev. A* **2014**, *89*, 022712. [CrossRef]
18. Boyle, G.J.; Muccignat, D.L.; Machacek, J.R.; McEachran, R.P. The influence of positron-Xe elastic scattering cross section variation on $\langle Z_{\mathrm{eff}} \rangle$ relaxation. *J. Phys. B At. Mol. Opt. Phys.* **2025**, *58*, 235201. [CrossRef]
19. Kramida, A.; Ralchenko, Y.; Reader, J.; NIST ASD Team. *NIST Atomic Spectra Database (Ver. 5.12)*; National Institute of Standards and Technology: Gaithersburg, MD, USA, 2024. Available online: https://physics.nist.gov/asd (accessed on 26 January 2026).
20. McEachran, R.; Stauffer, A. Positronium formation in the noble gases. *J. Phys. B At. Mol. Opt. Phys.* **2013**, *46*, 075203. [CrossRef]
21. Reid, D.D.; Wadehra, J. A quasifree model for the absorption effects in positron scattering by atoms. *J. Phys. B At. Mol. Opt. Phys.* **1996**, *29*, L127–L133. Erratum in *J. Phys. B At. Mol. Opt. Phys.* **1997**, *30*, 2318–2318. [CrossRef]
22. Salvat, F. Optical-model potential for electron and positron elastic scattering by atoms. *Phys. Rev. A* **2003**, *68*, 012708. [CrossRef]
23. Moore, C.E. *Atomic Energy Levels. As Derived from the Analyses of Optical Spectra*; Technical Report; U.S. Government Printing Office: Washington, DC, USA, 1958; Volume 3.
24. Kumar, K.; Skullerud, H.; Robson, R.E. Kinetic theory of charged particle swarms in neutral gases. *Aust. J. Phys.* **1980**, *33*, 343–448. [CrossRef]
25. Robson, R. Physics of reacting particle swarms in gases. *J. Chem. Phys.* **1986**, *85*, 4486–4501. [CrossRef]
26. Yousfi, M.; Segur, P.; Vassiliadis, T. Solution of the Boltzmann equation with ionisation and attachment: Application to SF 6. *J. Phys. D Appl. Phys.* **1985**, *18*, 359–375. [CrossRef]
27. Wright, G.L.; Charlton, M.; Griffith, T.C.; Heyland, G.R. The annihilation of positrons and positronium formation in gaseous Kr and Xe. *J. Phys. B At. Mol. Phys.* **1985**, *18*, 4327. [CrossRef]
28. Fraser, P. *Advances in Atomic and Molecular Physics*; Academic Press: New York, NY, USA, 1968; Volume 4, p. 63.
29. Machacek, J.; Blanco, F.; Garcia, G.; Buckman, S.; Sullivan, J. Regularities in positronium formation for atoms and molecules. *J. Phys. B At. Mol. Opt. Phys.* **2016**, *49*, 064003. [CrossRef]
30. Kim, Y.K.; Rudd, M.E. Binary-encounter-dipole model for electron-impact ionization. *Phys. Rev. A* **1994**, *50*, 3954–3967. [CrossRef]

31. McEachran, R.P.; Stauffer, A.D.; Campbell, L.E.M. Positron scattering from krypton and xenon. *J. Phys. B At. Mol. Phys.* **1980**, *13*, 1281. [CrossRef]
32. Robson, R.E.; Kumar, K. On the validity of the two-term approximation of the electron distribution function. *Aust. J. Phys.* **1971**, *24*, 835–840. [CrossRef]
33. White, R.D.; Robson, R.E.; Schmidt, B.; Morrison, M.A. Is the classical two-term approximation of electron kinetic theory satisfactory for swarms and plasmas? *J. Phys. D Appl. Phys.* **2003**, *36*, 3125. [CrossRef]
34. Petrović, Z.L.; Dujko, S.; Marić, D.; Malović, G.; Nikitović, Z.; Sasić, O.; Jovanović, J.; Stojanović, V.; Radmilović-Radjenović, M. Measurement and interpretation of swarm parameters and their application in plasma modelling. *J. Phys. D Appl. Phys.* **2009**, *42*, 194002. [CrossRef]
35. Brennan, M.; Ness, K. Momentum Transfer Cross Section for e–Kr Scattering. *Aust. J. Phys.* **1993**, *46*, 249–260. [CrossRef]
36. Green, D.G. Positron Cooling and Annihilation in Noble Gases. *Phys. Rev. Lett.* **2017**, *119*, 203403. [CrossRef]

Disclaimer/Publisher's Note: The statements, opinions and data contained in all publications are solely those of the individual author(s) and contributor(s) and not of MDPI and/or the editor(s). MDPI and/or the editor(s) disclaim responsibility for any injury to people or property resulting from any ideas, methods, instructions or products referred to in the content.